

LOCALISED AUXIN PEAKS IN CONCENTRATION-BASED TRANSPORT MODELS FOR PLANTS

DELPHINE DRAELANTS ^{*}, DANIELE AVITABILE [†], AND WIM VANROOSE [‡]

Abstract. We study the existence and bifurcation structure of stationary localised auxin spots in concentration-based auxin-transport models posed on one- and two-dimensional networks of plant cells. In regular domains with small active transport coefficient and no diffusion, the geometry of the cellular array encodes the peaks' height and location: asymptotic calculations show that peaks arise where cells have fewer neighbours, that is, at the boundary of the domain. We perform numerical bifurcation analysis for a concrete model available in literature and provide numerical evidence that the mechanism above remains valid in the presence of diffusion in both regular and irregular arrays. Using the active transport coefficient as bifurcation parameter, we find snaking branches of localised solutions, with peaks emerging from the boundary towards the interior of the domain. In one-dimensional regular arrays we observe oscillatory instabilities along the branch. In two-dimensional irregular arrays the snaking is slanted, hence stable localised solutions with peaks exist in a wide region of parameter space: the competition between active transport and production rate determines whether peaks remain localised or cover the entire domain.

Key words. Auxin transport models; Auxin patterns; Localised patterns; Snaking; Numerical Bifurcation Analysis

1. Introduction. The plant hormone auxin plays a crucial role in plant development [1, 2, 3, 4], yet the mechanisms through which it accumulates in certain cells and interacts with cellular growth remain largely unclear. The patterns formed during the growth of a plant are controlled by the local concentration of the hormone auxin in certain areas of the meristem. For example, it is known that the distribution of auxin maxima in the shoot apex gives rise to the formation of primordia [5, 6, 7]. Similarly, the distribution of auxin in the root tip coordinates cell division and cell expansion [8, 9]. In models of root hair initiation, intra-cellular levels and gradients of auxin concentration influence the localisation of G-proteins, which in turn promote hair formation [10]. In addition, it is known that the distribution of auxin in the leaf primordia mediates vascular patterning [1]. In recent years, many aspects of the molecular basis of these mechanisms have been unraveled and mathematical models of auxin transport have been proposed to explain growth and development [11, 12, 13, 14].

Computer simulation is typically used to compare the model output with observed data such as auxin distribution, venation patterns, growth or development. At cellular level, carriers such as PIN proteins, that are localized in the cell membrane, determine the rate and direction of auxin transport. The coordinated activity of many cells can create peaks of auxin that drive differentiation and growth. Various models that implement and refine these ideas have been proposed [8, 15, 16, 5, 7, 6, 17]. Such models differ primarily in the specifics of the transport and the coupling to the cell growth and division, but a common feature is that they support spatially-extended patterns of auxin concentration, which have also been observed experimentally.

Existing models can be classified into two main categories, *flux-based* and *concentration-*

^{*}Department of Mathematics and Computer Science, Universiteit Antwerpen, Middelheimlaan 1, B 2020, Antwerpen

[†]Centre for Mathematical Medicine and Biology, School of Mathematical Sciences, University of Nottingham, University Park, Nottingham, NG7 2RD, UK

[‡]Department of Mathematics and Computer Science, Universiteit Antwerpen, Middelheimlaan 1, B 2020, Antwerpen

based, depending on how auxin influences the localization of transport mediators (PINs) to form patterns. In flux-based models, first proposed in [18], the polarization depends on the net auxin flux between neighbouring cells: the higher the net flux towards the neighbours, the more PIN will accumulate at the membrane, and changes in the PIN distribution determine changes in auxin fluxes. By contrast, in concentration-based models it is assumed that the PIN accumulation on the membrane is caused by differences in auxin concentration between neighbouring cells. This type of models was introduced in [5] and [7]. For reviews on both flux- and concentration-based models we refer the reader to [19, 20, 21, 22].

Patterns in the models above are found by direct numerical simulation, upon choosing control parameters within a plausible biological range. However, there is still a large uncertainty on many of the parameter values which are often approximate [23, 24], adopted from different systems [25] or estimated with large error margins [26]. Furthermore, it is unclear what is the effect of systematic parameter variations on the generated patterns and how this relates to the behaviour of the biological system. In general, understanding the formation of auxin peaks from a dynamical system standpoint is still an open problem. Therefore a systematic exploration of the parameter variations can generate new hypotheses which can be experimentally validated and can provide more insight into pattern formation mechanisms [1, 27, 28].

In this paper we perform such exploration on a concentration-based auxin transport model, which is studied as a dynamical system using numerical bifurcation analysis [29]. In particular, we find steady states of the system and explore their dependence upon control parameters, investigating how patterns lose or gain stability in response to parameter changes. The aim is to predict qualitatively the distribution patterns that can occur for a certain parameter range and predict transitions between different types of patterns.

More precisely, we investigate the origin of localized peaks of auxin concentration in a model proposed by Smith et al. [5] and study the short time-scale effects of the active-transport coefficient, the diffusivity coefficient and the auxin production coefficient. This might help to explain how the maxima in a shoot apex are formed or how auxin coordinates cell division and cell expansion in a root tip.

The model proposed in [5] supports a homogeneous steady state that can be computed analytically for the idealized situation of spatially-extended arrays with periodic boundary conditions and identical cells. We show analytically that, in systems with finite size, solutions with localised peaks of auxin emerge from the homogeneous steady state for infinitesimal values of the active-transport parameter. In regular arrays, we find that geometry is a fundamental ingredient in the formation of auxin patterns, in that peaks arise naturally in cells that have fewest neighbours, towards the boundary of the domain. Importantly, we find that this mechanism occurs in a generic class of concentration-based models, of which the model presented in [5] is an example.

By employing numerical continuation techniques, we find that solutions with localised peaks at the boundary exist and are stable also for moderate and large values of the transport coefficient. Our analysis shows that such solutions are arranged in a *snaking bifurcation diagram*, a well-known characteristic of a wide variety of systems supporting localised states [30]. This bifurcation structure has been extensively studied in (systems of) nonlinear partial differential equations posed in one [31, 32, 33, 34, 35], two [36, 37] and three [38, 39] spatial dimensions, as well as in discrete [40] and nonlocal systems [41, 42, 43, 44]: solutions with one or more peaks in the middle of the domain undergo a series of saddle-node bifurcations, giving rise

to a hierarchy of steady states with an increasing number of bumps, all occurring in a well-defined range of parameter space.

When the system by Smith et al. is posed on a one-dimensional array of identical cells, steady state solutions with auxin peaks at the boundary undergo regular snaking and, as the bifurcation diagram is ascended, new peaks grow from the periphery towards the core of the domain. In addition, a similar scenario is found for two-dimensional, heterogeneous cellular arrays, and we argue that this mechanism could be a robust feature in several types of concentration-based auxin models.

The outline of the paper is as follows: In Section 2 we present the model for auxin transport, which is a large set of coupled nonlinear ordinary differential equations. We then discuss the results of the bifurcation analysis in Section 3, showing bifurcation diagrams and stability computations for regular 1D and 2D cellular arrays as well as an irregular 2D array. We present results mostly in the form of numerical simulations, while we collect in the supplementary material the corresponding analytical developments. We conclude in Section 4.

2. A mathematical model for auxin transport. We focus on concentration-based auxin transport models consisting of a system of nonlinear ordinary differential equations (ODEs) describing the time evolution of auxin concentrations and possibly PIN amounts. The ODEs are posed on a static, undirected graph where vertices represent cells and edges are drawn between adjacent cells (see the Supplementary Material for a formal definition). Concentration-based models possess an inherent time-scale separation: the growth hormone dynamics involve short time scales (of the order of seconds) [45], while changes in cellular shapes and proliferation of new cells occur on much slower time scales (hours or days) [46]. In this paper we concentrate on the fast time scale of hormone transport and hence consider plant organs as static cell structures.

Cells are identified with an index $i \in \{1, \dots, n\}$ and to each cell we associate a set of neighbours \mathcal{N}_i of cardinality $|\mathcal{N}_i|$, a volume V_i and a time-dependent auxin concentration $a_i(t)$. The rate of change of auxin concentration in each cell is expressed as a balance between auxin production and decay within the cell, diffusion towards neighbouring cells and active transport.

$$\begin{aligned} \frac{da_i}{dt} = & \pi(a_i) - \delta(a_i) + \frac{D}{V_i} \sum_{j \in \mathcal{N}_i} l_{ij} (a_j - a_i) \\ & + \frac{T}{V_i} \sum_{j \in \mathcal{N}_i} [P_{ji}(\mathbf{a}) f(a_j, a_i) - P_{ij}(\mathbf{a}) f(a_i, a_j)], \end{aligned} \quad (2.1)$$

for $i = 1, \dots, N$, where $\pi(\cdot)$ and $\delta(\cdot)$ model the auxin production and decay, respectively, $D \geq 0$ is a diffusion coefficient, and $l_{ij} \geq 0$ is a measure of the contact area between the adjacent cells i and j ; in addition, $T \geq 0$ is the active-transport coefficient, $P_{ij}(\cdot)$ is the number of PIN1 proteins located in the membrane of cell i toward the neighbouring cell j and $f(\cdot, \cdot)$ models the active transport as a saturable Michaelis-Menten mechanism.

In the simple model above, cells are characterised solely by their auxin concentration, but more realistic descriptions take into account other substances as well. For instance, transport mediators like the protein PIN1 are key players in active transport [47], hence we can assume that the function P_{ij} in Equation (2.1) depends upon the number of PIN1 proteins and the system can be closed with an additional ODE for the PIN1 rate of change.

A possible coupled model was proposed by Smith et al. [5], where the transport of the IAA hormone through the cells is modelled by describing the simultaneous evolution of PIN1 amounts and IAA concentrations [5]. It is assumed that the amount and localization of PIN1 depends on the IAA concentration in the cell and its neighbours. Further, Smith et al. assume that the IAA concentration changes as a result of fluxes that depend on PIN1 concentration and localisation. This results in a nonlinear feedback loop, which leads to the following set of ODEs

$$\begin{aligned} \frac{da_i}{dt} = & \frac{\rho_{\text{IAA}}}{1 + \kappa_{\text{IAA}}a_i} - \mu_{\text{IAA}}a_i + \frac{D}{V_i} \sum_{j \in \mathcal{N}_i} l_{ij}(a_j - a_i) \\ & + \frac{T}{V_i} \sum_{j \in \mathcal{N}_i} \left[P_{ji}(\mathbf{a}, \mathbf{p}) \frac{a_j^2}{1 + \kappa_T a_i^2} - P_{ij}(\mathbf{a}, \mathbf{p}) \frac{a_i^2}{1 + \kappa_T a_j^2} \right] \end{aligned} \quad (2.2)$$

$$\frac{dp_i}{dt} = \frac{\rho_{\text{PIN}_0} + \rho_{\text{PIN}}a_i}{1 + \kappa_{\text{PIN}}p_i} - \mu_{\text{PIN}}p_i \quad (2.3)$$

where p_i denotes the time-dependent PIN1 amount in cell i at time t and

$$P_{ij}(\mathbf{a}, \mathbf{p}) = p_i \frac{l_{ij} \exp(ca_j)}{\sum_{k \in \mathcal{N}_i} l_{ik} \exp(ca_k)}. \quad (2.4)$$

All model parameters are assumed to be strictly positive, with the exception of ρ_{PIN_0} , D and T which are nonnegative. We collect model parameters, units and reference values in Table 1 of the Supplementary Material.

Other types of coupled models are also possible: in particular, Jönsson et al. [7] propose a coupled model that includes PIN1 dependence on auxin efflux. This model assumes a feedback mechanism by which cells with relatively high auxin concentrations increase their auxin content by influencing PIN1 polarity in the neighbouring cells which, as a result, become auxin depleted. The model by Jönsson et al. features a system of 3 ODEs per cell.

Our methodology is applicable to a generic class concentration-based auxin transport models (see Supplementary Material for details), for which we expect similar qualitative results. We shall analyse in detail only the coupled model of Smith et al., given by Equations (2.2)–(2.4), but we stress that the framework presented here is applicable also to the model by Jönsson et al.

3. Results. As mentioned in the introduction, several examples in literature show patterns supported by concentration-based models for a particular choice of model parameters, whose values may be uncertain [5, 7]. As we shall see, parameter values have a profound effect on the solution landscape, therefore we aim to understand the origin and stability of auxin patterns by a systematic parameter variation.

Our main continuation parameter will be the active transport coefficient T . For $T \ll 1 \mu\text{m}^3/\text{h}$, diffusion dominates over transport while for large T the scenario is reversed. We shall first present results for a finite one-dimensional array of identical cells for $D = 0 \mu\text{m}^2/\text{h}$ and $T \ll 1 \mu\text{m}^3/\text{h}$: under these assumptions we derive analytical expressions of solution patterns with low-amplitude auxin peaks at the distal part of the domain. For D positive and larger values of T , we use numerical continuation, compute bifurcation diagrams and discuss instabilities that lead to the formation of additional peaks towards the core. We then extend our results to two-dimensional arrays of (possibly inhomogeneous) cells with nonzero diffusion. Finding analytical results for these systems is more cumbersome, but our numerical framework

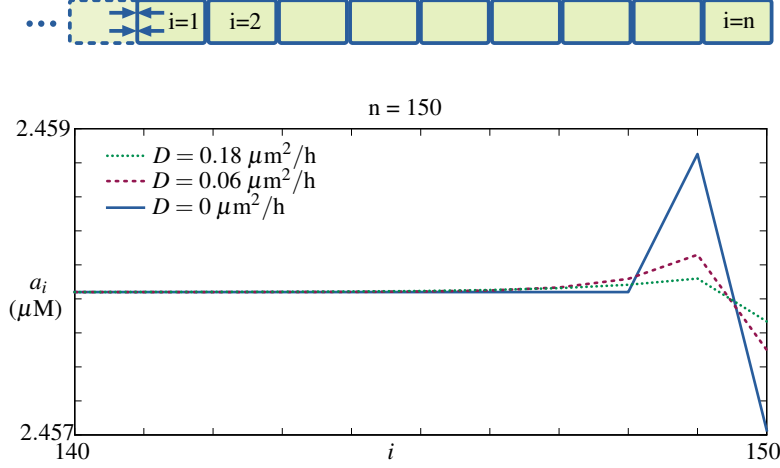


FIG. 3.1. *Top: geometry of a one-dimensional cellular array of identical cells with no-flux boundary conditions at $i = 1$ and free boundary conditions at $i = n$. This configuration can be seen as an idealisation of an unbranched plant root with proximal ($i = 1$) and distal ($i = n$) sides. Bottom: approximate solution pattern $a^* + T\alpha_i$ towards the boundary $i = n$ for $n = 150$ and various values of the diffusion coefficient. Parameters: $T = 3 \cdot 10^{-5} \mu\text{m}^3/\text{h}$, other parameters as in Table 1 in Supplementary Material.*

can easily be adapted from the one-dimensional case. We provide numerical evidence that the mechanism for the formation of auxin peaks remains substantially unaltered in these more realistic configurations.

3.1. Homogeneous steady state. Let us consider for simplicity an unbounded array of identical cells, all having an equal number of neighbours (alternatively, we could think of a periodic regular array). In order to find a homogeneous equilibrium we set $(a_i(t), p_i(t)) \equiv (a^*, p^*)$, for all cells i in model (2.2)–(2.3) and find

$$\begin{aligned} a_i = a^* &= \frac{-1 + \sqrt{1 + 4\kappa_{\text{IAA}}\rho_{\text{IAA}}/\mu_{\text{IAA}}}}{2\kappa_{\text{IAA}}} \\ p_i = p^* &= \frac{-1 + \sqrt{1 + 4\kappa_{\text{PIN}}(\rho_{\text{PIN}0} + \rho_{\text{PIN}}a^*)/\mu_{\text{PIN}}}}{2\kappa_{\text{PIN}}}. \end{aligned} \quad (3.1)$$

Even though the expressions above are valid only for the Smith et al. model, a similar homogeneous stationary solution could be found for more generic models, upon balancing production and decay terms in each ODE. In particular, this is valid for systems of type (2.1).

3.2. Small-amplitude solution in a finite one-dimensional domain. We now discuss the existence of inhomogeneous solution profiles in a finite one-dimensional array of identical cells. This configuration can be seen as an idealisation of an unbranched plant root, where the cells at $i = 1$ and $i = n$ constitute the proximal and distal parts, respectively (see Figure 3.1). In this setting, each cell has 2 neighbours, except the last cell, which has only 1 neighbour. At $i = 1$, we prescribe Neumann boundary conditions, that is, we assume zero net proximal flux via ghost cells; at $i = n$ we assume free boundary conditions, that is, we identify cell n with the root tip, so $\mathcal{N}_n = n - 1$. Both boundary conditions are widely used in literature. We remark that the free boundary condition at $i = n$ should not be confused with a zero

Dirichlet boundary condition, for which we would prescribe $\mathcal{N}_n = \{n-1, n+1\}$ and $a_{n+1}(t) \equiv p_{n+1}(t) \equiv 0$.

In this finite one-dimensional setting, the homogeneous solution (3.1) exists only for $T = 0 \mu\text{m}^3/\text{h}$, as for positive T the sums in the transport term do not vanish in general. However, asymptotic expressions for steady states in the Smith et al. model can be derived for $D = 0 \mu\text{m}^2/\text{h}$ and $T \ll 1 \mu\text{m}^3/\text{h}$. We seek patterns in the form of small deviations from the trivial solution, that is, $a_i = a^* + T\alpha_i + \mathcal{O}(T^2)$; an expansion of the vector-field around $(\mathbf{a}^*, \mathbf{p}^*)$ gives, to leading order (see Supplementary Material for a generic derivation)

$$\begin{aligned}
 a_i &= \begin{cases} a^* & \text{for } i = 1 \dots n-2, \\ a^* + \frac{p^*T}{2V} \left[\frac{\rho_{\text{IAA}}\kappa_{\text{IAA}}}{1 + \kappa_{\text{IAA}}(a^*)^2} + \mu_{\text{IAA}} \right]^{-1} \frac{(a^*)^2}{1 + \kappa_T(a^*)^2} & \text{for } i = n-1, \\ a^* - \frac{p^*T}{2V} \left[\frac{\rho_{\text{IAA}}\kappa_{\text{IAA}}}{1 + \kappa_{\text{IAA}}(a^*)^2} + \mu_{\text{IAA}} \right]^{-1} \frac{(a^*)^2}{1 + \kappa_T(a^*)^2} & \text{for } i = n. \end{cases} \\
 p_i &= \begin{cases} p^* & \text{for } i = 1, \dots, n-2, \\ p^* + \left[\frac{(\rho_{\text{PIN}_0} + \rho_{\text{PIN}}a^*)\kappa_{\text{PIN}}}{(1 + \kappa_{\text{PIN}}p^*)^2} + \mu_{\text{PIN}} \right]^{-1} \frac{\rho_{\text{PIN}}}{1 + \kappa_{\text{PIN}}p^*} (a_i - a^*) & \text{for } i = n-1, \\ p^* - \left[\frac{(\rho_{\text{PIN}_0} + \rho_{\text{PIN}}a^*)\kappa_{\text{PIN}}}{(1 + \kappa_{\text{PIN}}p^*)^2} + \mu_{\text{PIN}} \right]^{-1} \frac{\rho_{\text{PIN}}}{1 + \kappa_{\text{PIN}}p^*} (a_i - a^*) & \text{for } i = n. \end{cases} \tag{3.2}
 \end{aligned}$$

Therefore, for infinitesimal values of the transport coefficient T , the perturbed solution coincides with the trivial solution, except for a small peak at cell $n-1$ and a small dip at cell n (see also bold curve in Figure 3.1). We stress that the expressions above are easily generalised to regular two-dimensional arrays of identical cells, for which peaks are created close to cells with the fewest neighbours (see supplementary material and Section 3.7). This is a consequence of the fact that, if cells are identical and there is no diffusion, the geometry of the cellular array encodes the peaks position: more precisely, deviations from the trivial steady state are proportional to $\xi_i = 1 - \sum_{j \in \mathcal{N}_i} 1/|\mathcal{N}_j|$. A straightforward calculation shows that in the one-dimensional array $\xi_i = 0$ for $i = 0, \dots, n-2$ and $\xi_{n-1, n} = \mp 1/2$, which leads to the correction terms in Equation (3.2). In other words, peaks are present where the number of neighbours differs from the number of neighbours in the unbounded domain, that is, where the sum in the active transport in Equation (2.2) is nonzero. In the supplementary material we derive this result for a class systems with m ODEs in each cell and generic regular domains. We remark that the emergence of peaks in these models is not the consequence of an instability of the trivial state (as was found for non-localised states in [7]): solution profiles are stable for both $T = 0 \mu\text{m}^3/\text{h}$ (for which they are homogeneous) and for $T \ll 1 \mu\text{m}^3/\text{h}$ (for which they develop localised peaks).

3.3. Small-amplitude solution in the finite one-dimensional domain with diffusion. Asymptotic calculations can be carried out when T is small and $D = \mathcal{O}(T)$, leading to a linear system for the perturbations (see Supplementary Material), which can be computed analytically using Chebyshev polynomials [48] or numerically using linear algebra routines.

In Figure 3.1 we plot approximate steady states towards the boundary $i = n$ for $T = 3 \cdot 10^{-5} \mu\text{m}^3/\text{h}$ and various values of the diffusion coefficient. The boundary conditions are the same as in section 3.2. We notice that, in the regime of small

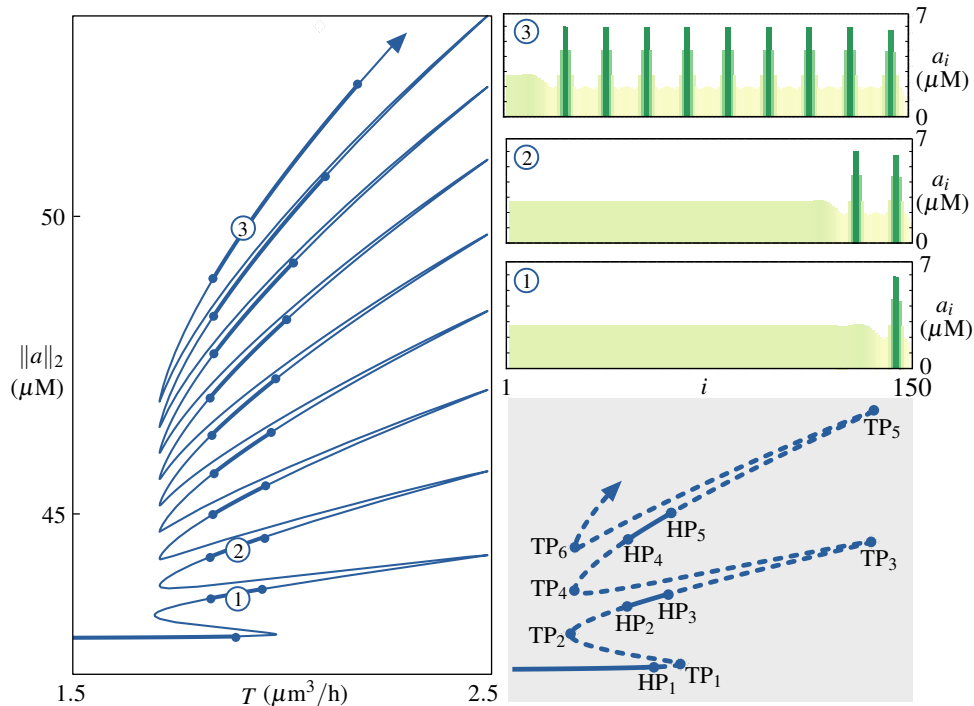


FIG. 3.2. *Bifurcation diagram and selected solution patterns for the Smith et al. model posed on a row of 150 identical cells with Neumann boundary conditions at $i = 1$ and free boundary conditions at $i = n$. Left: 2-norm of auxin concentration versus active transport parameter T . Right: as the snaking bifurcation diagram is ascended, new peaks are formed from the boundary towards the interior. Bottom-right: stable segments of the branch are found between Hopf bifurcations HP_2 and HP_3 , HP_4 and HP_5 , etc. Other secondary instabilities (not shown) are present along the unstable branches. Parameters are reported in Table 1 of the Supplementary Material.*

active transport and comparatively much bigger diffusion coefficient, a peak is still present at the boundary. Inspecting the solid line ($D = 0 \mu\text{m}^2/\text{h}$) and the dashed lines ($D = 0.06 \mu\text{m}^2/\text{h}$ and $D = 0.18 \mu\text{m}^2/\text{h}$) we see that the peaks decrease in amplitude and are more spread out, as expected.

3.4. Snaking continuation curve. In realistic simulations the transport coefficient T is not necessarily small [5, 7], therefore it is interesting to explore what happens to the small-amplitude inhomogeneous solution found in Section 3.2 when we increase active transport in the presence of diffusion. This is done using numerical bifurcation analysis, that is, equilibria of system (2.2)–(2.3) are followed in parameter space using Newton–Raphson method and pseudo-arclength continuation [29]. Linear stability is then inferred computing the spectrum of the Jacobian at the steady state.

In Figure 3.2 we show a branch of solutions for a one-dimensional domain with $n = 150$, Neumann boundary conditions at $i = 1$, free boundary conditions at $i = n$ and control parameters specified in Table 1 of the Supplementary Material. We start the computation from the homogeneous solution at $T = 0$ and follow the pattern for increasing values of T . As T changes, we plot the 2-norm of the auxin vector, $\|\mathbf{a}\|_2$, which is a measure of the spatial extent of the solution (the lower $\|\mathbf{a}\|_2$, the more localised the pattern) and denote stable (unstable) branches with solid (dashed) or thick (thin) lines.

The peak found in the neighbourhood of the distal boundary persists for increasing values of T and grows steadily until we meet a first turning point (TP1). The analytic asymptotic profile (3.2) gives a relative error $\|\mathbf{a} - (\mathbf{a}^* + T\boldsymbol{\alpha})\|_2 / \|\mathbf{a}\|_2$ less than 0.4% for $T \leq 0.2 \mu\text{m}^3/\text{h}$ (see Supplementary Material), after which higher-order terms become predominant.

As we ascend the bifurcation diagram, new peaks are formed from the distal towards the proximal part of the domain, until the domain is filled with peaks. This bifurcation diagram resembles the one found for reaction–diffusion PDEs posed on the real line [32, 33, 34] except that here peaks are formed at the boundary rather than at the core of the domain. When peaks fill the entire domain, the branch enters an unstable irregular regime without snaking (not shown). Branches of solutions with peaks covering the entire domain are also present (not shown) and are partially discussed in Section 3.6

3.5. Instabilities on the snaking branch. The Jacobian matrix for the spatially-extended system (2.2)–(2.3) is sparse with a characteristic block structure determined by transport and diffusion terms (we refer the reader to [49] for a detailed description) and, for relatively small systems such as this one, eigenvalues are computed with dense linear algebra.

The solution with one small peak at the boundary becomes unstable at a Hopf bifurcation (HP1) at $T \approx 2.1 \mu\text{m}^3/\text{h}$, closely followed by other oscillatory instabilities and a saddle-node bifurcation (TP1) at $T \approx 2.2 \mu\text{m}^3/\text{h}$, after which the solution remains unstable. On the snaking branch, we find that saddle-node and Hopf bifurcations alternate regularly, as documented in Figure 3.2: saddle-node bifurcations align at $T \approx 1.9 \mu\text{m}^3/\text{h}$ and $T \approx 2.5 \mu\text{m}^3/\text{h}$, while Hopf bifurcations depart from each other as patterns become less localised. In this parameter setting, stable portions of the branch are delimited by two Hopf bifurcations, which, to the best of our knowledge, has not been reported before for snaking in reaction–diffusion systems. It should be noted, however, that Burke and Dawes [50] found Hopf bifurcations at the bottom of the snaking branch for an extended Swift–Hohenberg equation, which may lead to a bifurcation structure similar to the one in Figure 3.2 if secondary parameters are varied.

In Figure 3.3 we show spectra of steady states at selected points on the branch. Overall these spectra resemble those found in discretised advection-diffusion PDEs, with largely negative real eigenvalues associated with diffusion terms of the governing equations. In this context, however, increasing the number of cells does not alter the cell spacing, hence the spectrum does not grow in the negative real direction for larger system sizes.

We monitored spectra of localised solutions as the snaking branch was ascended (see Figure 3.3): immediately after the Hopf bifurcation HP1, multiple eigenvalues cross the imaginary axis, therefore several oscillatory instabilities exist between HP1 and TP1 (HP2 and TP2, etc.). In the bottom panel of Figure 3.3 we show that the Hopf eigenfunction at HP1 has a maximum at the root tip and the one for HP2 is also spatially localised. We expect that branches of time-periodic (possibly spatially-localised) solutions emerge from the Hopf bifurcations. We have not observed stable small-amplitude oscillations in direct numerical simulations, but we report the existence of stable periodic states in which a temporal oscillation of the peak at $i = n$ initiates a wave of auxin moving towards the boundary at $i = 1$, with long oscillation periods (see Supplementary Material). It was recently shown by Farcot and Yuan that, in one-dimensional flux-based models with no-flux boundary conditions, active

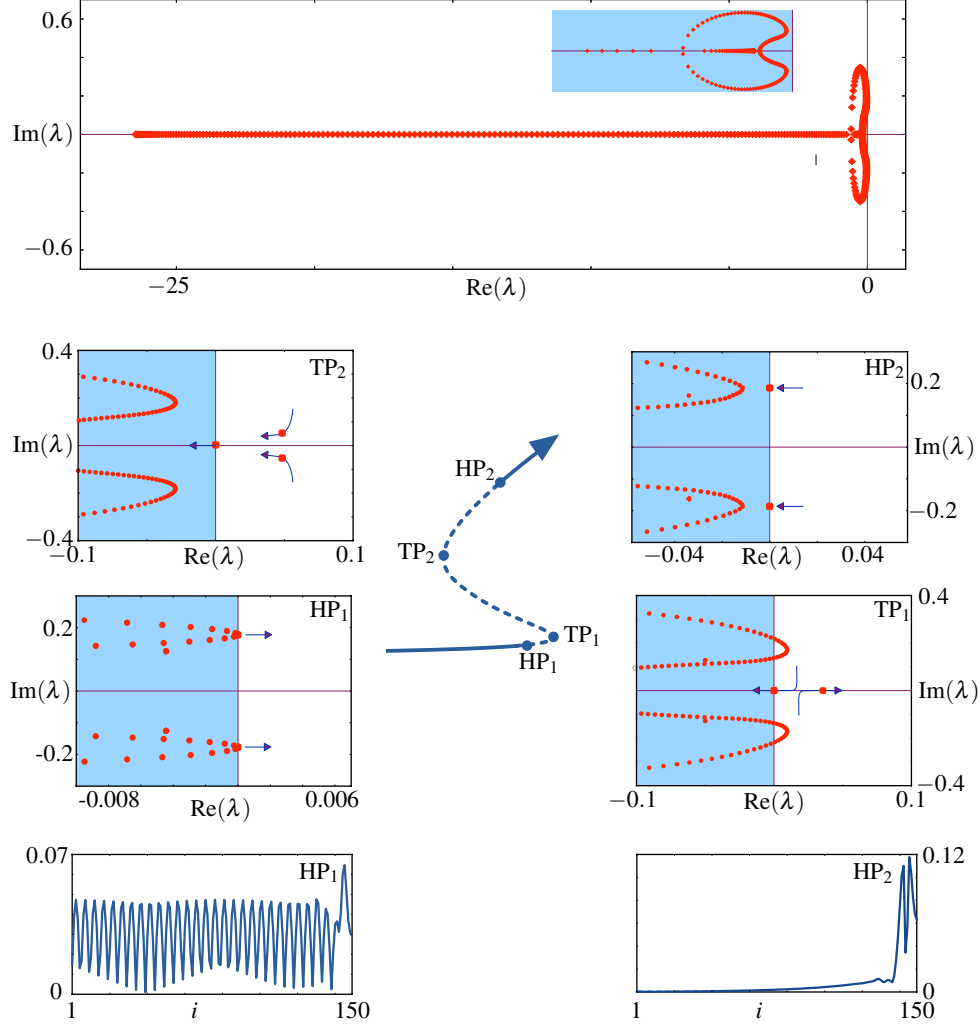


FIG. 3.3. *Spectral computations at selected solution profiles. Top: spectrum of a stable solution point for $T < T_{HP_1}$. Middle: spectra at selected bifurcation points found as the snaking bifurcation branch of Figure 3.2 is ascended. Bottom: unstable eigenfunctions at HP_1 and HP_2 . Parameters as in Figure 3.2.*

transport is sufficient to elicit auxin oscillations [51]. In the concentration-based model considered here, oscillatory states in regular one-dimensional arrays are also found in a regime where active transport dominates over diffusion.

3.6. Changes in the auxin production parameter. In [49] it was shown that the auxin production parameter ρ_{IAA} has a significant influence on the solution profiles, therefore it is interesting to study how changes in this parameter affect the bifurcation structure. We repeated the numerical continuation for 20 values of ρ_{IAA} in the interval $[0.3 \mu\text{M/h}, 1.5 \mu\text{M/h}]$. For low values of ρ_{IAA} , both the oscillatory instability HP_1 and the saddle node TP_1 move to the right and give rise to snaking bifurcation diagrams with increasingly wider stable segments (see Figure 3.4). In the limit $\rho_{IAA} \ll \mu_{IAA}$ decay dominates over production, hence large peaks can not be

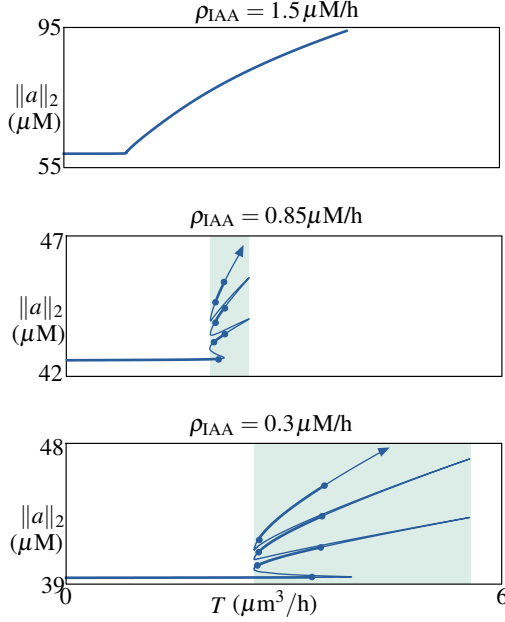


FIG. 3.4. Bifurcation diagram for various values of the auxin production coefficient ρ_{IAA} . Other parameters as in Figure 3.2. The lower the ρ_{IAA} , the wider the snaking width and the stable branches. For sufficiently large values of ρ_{IAA} the snaking disappears and peaks form at once on a fully stable branch.

sustained and indeed we find that the solution with a single peak at the tip persists for very large values of T and does not coexist with multi-peaked solutions.

On the other hand, increasing ρ_{IAA} causes the snaking diagram to shrink and then disappear for $\rho_{IAA} \geq 1.2 \mu\text{M/h}$. In Figure 3.4, we show a fully stable branch for $\rho_{IAA} = 1.5 \mu\text{M/h}$. On this branch peaks develop at once from the small-amplitude solution, without turning points. We mention however that for $\rho_{IAA} = 1.2 \mu\text{M/h}$ and $1.3 \mu\text{M/h}$, Hopf bifurcations are found along the non-snaking branch (not shown), similar to what is found for the infinite domain [49].

As snaking branches distort, several types of secondary instabilities and collisions with neighbouring branches occur. In particular, we report codimension-2 Bogdanov–Takens bifurcations originating from the collision between TP2 and HP2, (TP4 and HP4, TP6 and HP6, etc.) when ρ_{IAA} is varied. The existence of these codimension-2 bifurcations could also be envisaged inspecting the spectra in Figure 3.3.

3.7. Two-dimensional domains. The methods described above are readily adapted to two-dimensional domains. We studied two cases: a tessellation of regular hexagonal cells and a realistic domain with irregular shaped cells. In both cases we use free boundary conditions.

In the first example we consider a rectangular domain of 50 by 50 hexagonal cells with 6 neighbours in the interior, 3 neighbours at the left and right edges and 4 neighbours at the top and bottom edges (see Figure 3.5). This example illustrates the influence of the number of neighbouring cells on the emerging patterns. In this geometry, corners have slightly different configurations and our asymptotic analysis for $D = 0 \mu\text{m}^2/\text{h}$ predicts the formation of peaks at the boundaries, with the highest peak at the top-left and bottom-right corners. Numerical computations for positive

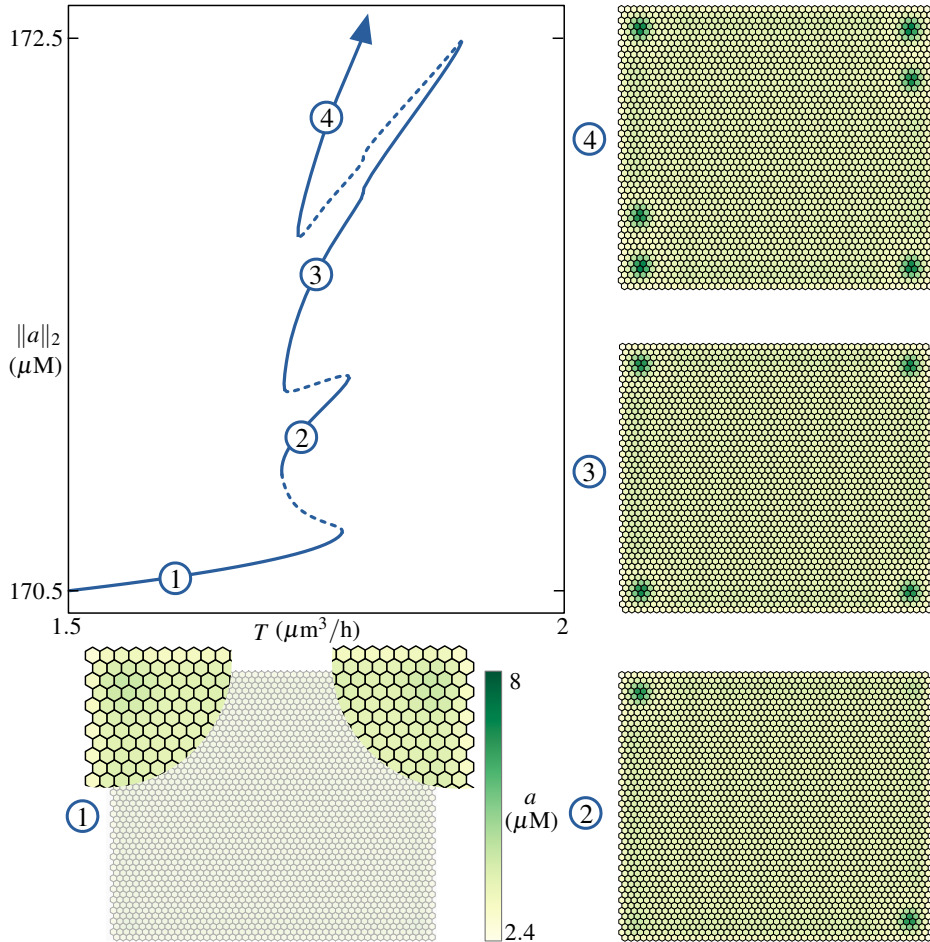


FIG. 3.5. Bifurcation diagram and selected solution patterns for the Smith et al. model posed on a regular array of 50 by 50 hexagonal cells with 6 neighbours in the interior, 3 neighbours at the left and right edge and 4 neighbours at the top and bottom edge. Larger peaks are developed initially at the top-left and bottom-right corner and new peaks are formed along the left and right edges, where we have fewer neighbours. Control parameters as reported in Table 1 of the Supplementary Material.

D show that these peaks persist and become prominent for increasing T . As in the one-dimensional case, patterns are arranged on a snaking bifurcation branch, even though in two-dimensions the snaking is slanted. Furthermore, after peaks arise in all four corners, new spots are formed initially along the left and right edges (where cells have fewer neighbours), and then, for sufficiently large values of ρ_{IAA} , along the top and bottom edges. In contrast to the one-dimensional case, we have not found oscillatory bifurcations in this region of parameter space, so we conclude that stable portions of the branch are now delimited by turning points (see Figure 3.5).

In the second example, 742 irregular cells cover an almost-circular domain in a realistic geometry (taken from [52]). Even though the asymptotic analysis is not valid for irregular arrays, we expect results to be qualitatively similar if cellular volumes and contact areas do not vary greatly from cell to cell. In this example the number of neighbours varies over the domain; however, the cells at the boundaries have,

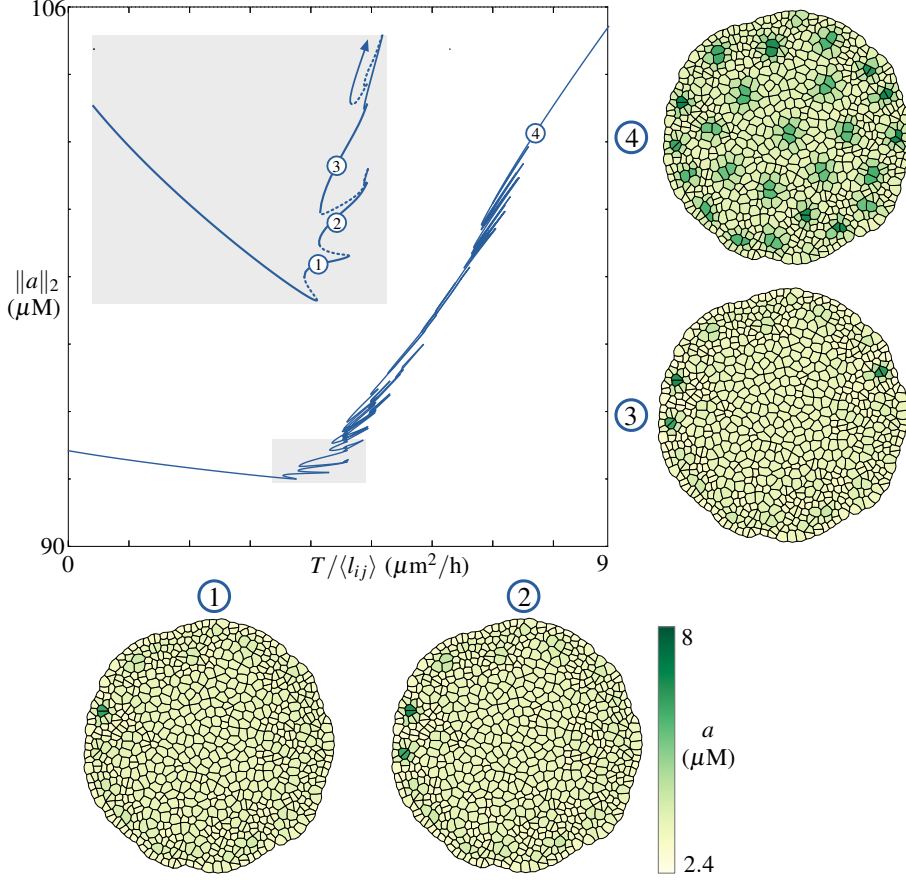


FIG. 3.6. Bifurcation diagram and selected solution patterns for the Smith *et al.* model for an almost-circular domain of 742 irregular cells (geometry taken from [52]). We find an irregular and slanted bifurcation diagram with stable portion delimited by saddle-nodes bifurcations. Control parameters as reported in Table 1 of the Supplementary Material.

predominantly, fewer neighbours and this is where peaks are formed initially. In this case, the bifurcation diagram is plotted in terms of the scaled bifurcation parameter $T/\langle l_{ij} \rangle$, where $\langle l_{ij} \rangle$ is the average contact surface. We note that in the regular domain $\langle l_{ij} \rangle = 1 \mu\text{m}$, whereas in the irregular domain $\langle l_{ij} \rangle \approx 13.26 \mu\text{m}$. As in the first example, stable portions of the branch are enclosed between consecutive saddle-nodes bifurcation and there are no oscillatory instabilities on the stable branches. Importantly, the slanted snaking ensures the (co-)existence of stable solutions with localised peaks for all realistic values of the parameter T .

4. Conclusion. In this paper we studied how auxin peaks arise in concentration-based cellular models over short time scales and showed how solution patterns are affected by changes in active transport and auxin production parameters.

In the absence of diffusion, a straightforward asymptotic analysis was carried out to explore the formation of spots of high auxin concentration. Such asymptotic analysis is valid for a class of models with identical cells and weak active transport, and it shows that peaks emerge as boundary corrections to the homogeneous steady state: the peak amplitude is proportional to coefficients that depend on the local

geometry and are higher in regions where cells have fewer neighbours, that is, next to the boundary. This mechanism provides a possible explanation of the origin of localised patterned states in auxin transport [53] and it shows that active transport promotes localisation for this class of models.

The model by Smith et al. [5] fits in the framework discussed above and, for this system, we have provided numerical evidence that the mechanism for the formation of auxin peaks remains substantially unaltered in the presence of diffusion for regular arrays. The transition between the flat state at zero active transport and solutions with small-amplitude peaks (localised at the boundary) does not involve a bifurcation of the trivial steady state (as it is usually found in reaction–diffusion PDEs).

The analysis mentioned above is directly applicable to other concentration-based models [7, 6] and could be extended to more detailed systems [17]. Common between all these models is that the active transport depends on the number of neighbours and as a result the deviations from the trivial state will again appear at the boundaries where the number of neighbours differs from the interior of the organ.

For intermediate values of active transport rate T , large-amplitude peaks are arranged on a snaking branch (regular snaking on one-dimensional arrays, slanted on two-dimensional arrays). From a biological perspective, this means that auxin peaks are formed robustly in the system and that stable patterns with variable number of peaks can coexist in the same parameter range. Importantly, we find that variations in the auxin production rate have a deep impact on the solution landscape: the results in Figure 3.4 support the conclusion that if auxin production rate was decreased quasi-statically (either actively, or passively), the organism would be able to switch from fully-patterned states to configurations with few peaks at the boundary.

When the Smith et al. model is posed on an irregular domain, the asymptotic analysis is not applicable but we found that the geometric argument for the peak formation is still valid, in that auxin peaks are formed close to the boundary for low values of the active transport parameter. However, we can not exclude a priori that auxin spots will form in the meristematic zone as a direct consequence of heterogeneities in cellular volumes and contact areas. A statistical characterisation of these quantities and their influence on peaks location is still an open problem, it is plausible that snaking will continue to occur preferentially at the boundary for sufficiently low variability of the control parameters.

Acknowledgements. We acknowledge fruitful discussions with Gerrit T.S. Beemster, Jan Broeckhove, Dirk De Vos, Abdiravuf Dzhurakhalov, Etienne Farcot and Przemysław Klosiewicz. DD acknowledges financial support from the Department of Mathematics and Computer Science of the University of Antwerp. DA acknowledges the University of Nottingham Research Development Fund, supported by the Engineering and Physical Sciences Research Council (EPSRC).

5. Supplementary Material.

5.1. Model parameters. We report here a brief description of model parameters, together with characteristic values and units, for the model of Smith et al. (see main text for details). In Table 5.1 we write default values for the simulations and we point out that some parameters vary during numerical computations: in the main text we discuss variations in active transport parameter T , auxin diffusion coefficient D and auxin production coefficient ρ_{IAA} . In addition, we point out that cellular volumes and contact areas change depending on the geometry: we have $V_i = 1 \mu\text{m}^3$, $l_{ij} = 1 \mu\text{m}$ (for 1D array of square cells) $V_i = 3\sqrt{3} \mu\text{m}^3$, $l_{ij} = 1 \mu\text{m}$ (for 2D array of hexagonal

cells) and $\langle l_{ij} \rangle = 13.26 \mu\text{m}$ (for the 2D irregular array, taken from Merks et al. [21]).

TABLE 5.1
Characteristic parameters of the Smith et al. model

Symbol	Description	Value	Unit
c	controls PIN distribution	1.099	$1/\mu\text{M}$
κ_{PIN}	PIN saturation coefficient	1.000	$1/\mu\text{M}$
κ_T	Transport saturation coefficient	1.000	
κ_{IAA}	IAA saturation coefficient	1.000	$1/\mu\text{M}$
ρ_{PIN_0}	Base production of PIN	0.000	$\mu\text{M}/\text{h}$
ρ_{PIN}	PIN production coefficient	1.000	$1/\text{h}$
μ_{PIN}	PIN decay coefficient	0.100	$1/\text{h}$
μ_{IAA}	IAA decay coefficient	0.100	$1/\text{h}$
ρ_{IAA}	IAA production coefficient	0.850 (1D) 1.500 (2D)	$\mu\text{M}/\text{h}$ $\mu\text{M}/\text{h}$
D	IAA diffusion coefficient	1.000	$\mu\text{m}^2/\text{h}$
T	IAA transport coefficient	1.000	$\mu\text{m}^3/\text{h}$

6. Asymptotic derivation of peak solutions. We begin by defining a generic concentration-based model without diffusion.

DEFINITION 6.1 (Concentration-based model without diffusion). *A concentration-based model without diffusion is a set of mn ODEs of the form*

$$\dot{\mathbf{y}}_i = \boldsymbol{\pi}(\mathbf{y}_i) - \boldsymbol{\delta}(\mathbf{y}_i) + T \sum_{j \in \mathcal{N}_i} \boldsymbol{\nu}_{ji}(\mathbf{y}_1, \dots, \mathbf{y}_n) - \boldsymbol{\nu}_{ij}(\mathbf{y}_1, \dots, \mathbf{y}_n), \quad i = 1, \dots, n, \quad (6.1)$$

where $\boldsymbol{\pi}, \boldsymbol{\delta}: \mathbb{R}_+^m \rightarrow \mathbb{R}_+^m$, are the production and decay functions, respectively, $T \in \mathbb{R}_+$, is the (nonnegative) active transport parameter, $\{1, \dots, n\}$ are vertices of a static undirected graph G , $\mathcal{N}_i \subseteq \{1, 2, \dots, n\}$ is the set of neighbours of cell i , containing $|\mathcal{N}_i|$ elements and $\boldsymbol{\nu}_{ij}: \mathbb{R}_+^m \times \dots \times \mathbb{R}_+^m \rightarrow \mathbb{R}_+^m$ are the active transport functions. We will assume $\boldsymbol{\pi}$, $\boldsymbol{\delta}$ and $\boldsymbol{\nu}_{ij}$ to be smooth vector fields depending on a set control parameters $\mathbf{p} \in \mathbb{R}_+^p$, but we omit this dependence for simplicity and write, for instance, $\boldsymbol{\pi}(\mathbf{y}_i)$ instead of $\boldsymbol{\pi}(\mathbf{y}_i; \mathbf{p})$.

We can then prove the following result:

LEMMA 6.1. *Let us consider the concentration-based model (6.1) and let us suppose that there exist vector-valued functions $\boldsymbol{\psi}: \mathbb{R}_+^m \times \mathbb{R}_+^m \rightarrow \mathbb{R}_+^m$ and $\boldsymbol{\varphi}: \mathbb{R}_+^m \rightarrow \mathbb{R}_+^m$ such that*

$$\boldsymbol{\nu}_{ij}(\mathbf{y}_1, \dots, \mathbf{y}_n) = \boldsymbol{\psi}(\mathbf{y}_i, \mathbf{y}_j) \odot \boldsymbol{\varphi}(\mathbf{y}_i) \oslash \sum_{k \in \mathcal{N}_i} \boldsymbol{\varphi}(\mathbf{y}_k), \quad \text{for all } i, j = 1, \dots, n, \quad (6.2)$$

where \odot and \oslash denote the standard Hadamard product and division between vectors. Further, let $\mathbf{y}^* \in \mathbb{R}^m$ be such that $\boldsymbol{\pi}(\mathbf{y}^*) = \boldsymbol{\delta}(\mathbf{y}^*)$ and $\boldsymbol{\psi}(\mathbf{y}^*, \mathbf{y}^*) \neq \mathbf{0}$, then

1. If $T = 0$ or all cells have the same number of neighbours, $|\mathcal{N}_i| = |\mathcal{N}^*|$, then the homogeneous solution $(\mathbf{y}^*, \dots, \mathbf{y}^*)^T \in \mathbb{R}^{nm}$ is a steady state for the concentration-based model.
2. If $0 < T \ll 1$ and cells have different number of neighbours and the Jacobian matrix $\boldsymbol{\pi}'(\mathbf{y}^*) - \boldsymbol{\delta}'(\mathbf{y}^*)$ is nonsingular, then a inhomogeneous steady state to leading order is given by

$$\mathbf{y}_i = \mathbf{y}^* + \xi_i T [\boldsymbol{\pi}'(\mathbf{y}^*) - \boldsymbol{\delta}'(\mathbf{y}^*)]^{-1} \boldsymbol{\psi}(\mathbf{y}^*, \mathbf{y}^*), \quad i = 1, \dots, n$$

where the coefficients ξ_i depend on the local properties of the cellular array, namely

$$\xi_i = 1 - \sum_{j \in \mathcal{N}_i} \frac{1}{|\mathcal{N}_j|}.$$

Proof. If $T = 0$ the statement is clearly true, so henceforth we assume $T \neq 0$. Evaluating the sums in the right-hand side of (6.1) at the homogeneous solution gives

$$\begin{aligned} & \sum_{j \in \mathcal{N}_i} \nu_{ji}(\mathbf{y}^*, \dots, \mathbf{y}^*) - \nu_{ij}(\mathbf{y}^*, \dots, \mathbf{y}^*) \\ &= \sum_{j \in \mathcal{N}_i} \left(\psi(\mathbf{y}^*, \mathbf{y}^*) \odot \varphi(\mathbf{y}^*) \oslash \sum_{k \in \mathcal{N}_j} \varphi(\mathbf{y}^*) - \psi(\mathbf{y}^*, \mathbf{y}^*) \odot \varphi(\mathbf{y}^*) \oslash \sum_{k \in \mathcal{N}_i} \varphi(\mathbf{y}^*) \right) \\ &= \psi(\mathbf{y}^*, \mathbf{y}^*) \sum_{j \in \mathcal{N}_i} \left(\frac{1}{|\mathcal{N}_j|} - \frac{1}{|\mathcal{N}_i|} \right), \\ &= -\xi_i \psi(\mathbf{y}^*, \mathbf{y}^*) \end{aligned} \tag{6.3}$$

Since $\boldsymbol{\pi}(\mathbf{y}^*) - \boldsymbol{\delta}(\mathbf{y}^*) = \mathbf{0}$, the right-hand side of (6.1) vanishes for all i if $|\mathcal{N}_i| = |\mathcal{N}_j| = |\mathcal{N}^*|$. On the other hand, if not all cells have the same number of neighbours and T is small, we may seek for asymptotic steady states in the form $\mathbf{y}_i = \mathbf{y}^* + T\boldsymbol{\eta}_i + \mathcal{O}(T^2)$ for $i = 1, \dots, n$ and $(\boldsymbol{\eta}_i)_j = \mathcal{O}(1)$. A Taylor expansion of the right-hand side around $(\mathbf{y}^*, \dots, \mathbf{y}^*)^T \in \mathbb{R}^{nm}$ gives, to leading order,

$$\mathbf{0} = \boldsymbol{\pi}(\mathbf{y}^*) - \boldsymbol{\delta}(\mathbf{y}^*) + T[\boldsymbol{\pi}'(\mathbf{y}^*) - \boldsymbol{\delta}'(\mathbf{y}^*)]\boldsymbol{\eta}_i + T \sum_{j \in \mathcal{N}_i} \nu_{ji}(\mathbf{y}^*, \dots, \mathbf{y}^*) - \nu_{ij}(\mathbf{y}^*, \dots, \mathbf{y}^*),$$

and using (6.3) we obtain the assert. \square

REMARK 6.1 (Small-amplitude peak solutions). *In finite regular arrays, cells in the interior have all the same number of neighbours, so we can use these properties to give formal definitions of interior and boundary sets*

$$\begin{aligned} \mathcal{I} &= \left\{ i \in \{1, \dots, n\} \mid 1 - \sum_{j \in \mathcal{N}_i} \frac{1}{|\mathcal{N}_j|} = 0 \right\}, \\ \mathcal{B} &= \{1, \dots, n\} \setminus \mathcal{I}. \end{aligned}$$

In passing, we note that \mathcal{B} contains in general more cells than the physical boundary. Lemma 6.1 shows that, to leading order, steady states for small T deviate from the homogeneous solutions only in \mathcal{B} , where auxin peaks and dips are proportional to T and ξ_i , namely

$$\mathbf{y}_i = \begin{cases} \mathbf{y}^* & \text{if } i \in \mathcal{I}, \\ \mathbf{y}^* + \xi_i T [\boldsymbol{\pi}'(\mathbf{y}^*) - \boldsymbol{\delta}'(\mathbf{y}^*)]^{-1} \psi(\mathbf{y}^*, \mathbf{y}^*) & \text{if } i \in \mathcal{B}. \end{cases} \tag{6.4}$$

REMARK 6.2 (Irregular domains). *Lemma 2.1 can not be applied in general if the domain is irregular, that is, if cells have different volumes and contact lengths: if, say, the active transport function ν_{ij} depends explicitly on the cellular volume V_i and the V_i are not all equal, then it is not possible to express ν_{ij} as in (6.2).*

6.0.1. One-dimensional domain and one component per cell. As an example, we consider the Smith et al. model with constant fixed PIN amount, posed on a one-dimensional array of identical cells with volume V , Neumann boundary conditions at $i = 1$ and free boundary conditions at $i = n$. As pointed out in the main text, Neumann boundary conditions are obtained by considering ghost cells. Therefore boundary and interior sets are given by $\mathcal{I} = 1, \dots, n-2$ and $\mathcal{B} = \{n-1, n\}$, respectively. Furthermore we denote by p the fixed PIN concentration and apply Lemma 6.1 with $m = 1$, $y_i = a_i$ and

$$\begin{aligned}\pi: a &\mapsto \frac{\rho_{\text{IAA}}}{1 + \kappa_{\text{IAA}} a}, & \delta: a &\mapsto -\mu_{\text{IAA}} a, \\ \psi: (a, b) &\mapsto \frac{p}{V} \frac{a^2}{1 + \kappa_T b^2}, & \varphi: a &\mapsto \exp(ca),\end{aligned}$$

where all parameters are assumed to be strictly positive. By balancing production and decay terms we find the positive homogeneous state

$$a^* = \frac{-1 + \sqrt{1 + 4\kappa_{\text{IAA}}\rho_{\text{IAA}}/\mu_{\text{IAA}}}}{2\kappa_{\text{IAA}}}.$$

In the absence of active transport, a^* is a stable steady state of the model since $\pi'(a^*) - \delta'(a^*) < 0$. For $T \ll 1 \mu\text{m}^3/\text{h}$, \mathbf{a}^* is not a steady state since \mathcal{B} is nonempty and $\xi_{n-1} = -1/2$, $\xi_n = 1/2$, hence we obtain, to leading order

$$a_i = \begin{cases} a^* & \text{for } i = 1 \dots n-2, \\ a^* + \frac{pT}{2V} \left[\frac{\rho_{\text{IAA}}\kappa_{\text{IAA}}}{1 + \kappa_{\text{IAA}}(a^*)^2} + \mu_{\text{IAA}} \right]^{-1} \frac{(a^*)^2}{1 + \kappa_T(a^*)^2} & \text{for } i = n-1, \\ a^* - \frac{pT}{2V} \left[\frac{\rho_{\text{IAA}}\kappa_{\text{IAA}}}{1 + \kappa_{\text{IAA}}(a^*)^2} + \mu_{\text{IAA}} \right]^{-1} \frac{(a^*)^2}{1 + \kappa_T(a^*)^2} & \text{for } i = n. \end{cases}$$

6.0.2. One-dimensional domain and two components per cell. The Smith et al. model features 2 ODEs per cell. If we pose this model on a one-dimensional array of identical cells, the graph G associated to the nodes is the same of our previous example, hence \mathcal{B} , \mathcal{I} and ξ are unchanged. We can now apply Lemma 6.1 with $m = 2$, $\mathbf{y}_i = (a_i, p_i)^T$ and

$$\begin{aligned}\pi: \begin{bmatrix} a \\ p \end{bmatrix} &\mapsto \begin{bmatrix} \frac{\rho_{\text{IAA}}}{1 + \kappa_{\text{IAA}} a} \\ \frac{\rho_{\text{PIN}0} + \rho_{\text{PIN}} a}{1 + \kappa_{\text{PIN}} p} \end{bmatrix}, & \delta: \begin{bmatrix} a \\ p \end{bmatrix} &\mapsto \begin{bmatrix} -\mu_{\text{IAA}} a \\ -\mu_{\text{PIN}} p \end{bmatrix}, \\ \psi: \left(\begin{bmatrix} a \\ p \end{bmatrix}, \begin{bmatrix} b \\ q \end{bmatrix} \right) &\mapsto \begin{bmatrix} \frac{p}{V} \frac{a^2}{1 + \kappa_T b^2} \\ 0 \end{bmatrix}, & \varphi: \left(\begin{bmatrix} a \\ p \end{bmatrix} \right) &\mapsto \begin{bmatrix} \exp(ca) \\ 0 \end{bmatrix}.\end{aligned}$$

Balancing production and decay terms we find a homogeneous strictly positive steady state for $T = 0$

$$\mathbf{y}^* = \begin{bmatrix} a^* \\ b^* \end{bmatrix} = \begin{bmatrix} \frac{-1 + \sqrt{1 + 4\kappa_{\text{IAA}}\rho_{\text{IAA}}/\mu_{\text{IAA}}}}{2\kappa_{\text{IAA}}} \\ \frac{-1 + \sqrt{1 + 4\kappa_{\text{PIN}}(\rho_{\text{PIN}0} + \rho_{\text{PIN}} a^*)/\mu_{\text{PIN}}}}{2\kappa_{\text{PIN}}} \end{bmatrix}$$

which is stable since

$$\text{Spec}(\boldsymbol{\pi}'(\mathbf{y}^*) - \boldsymbol{\delta}'(\mathbf{y}^*)) = \left\{ -\frac{\rho_{\text{IAA}}\kappa_{\text{IAA}}}{(1 + \kappa_{\text{IAA}}a^*)^2} - \mu_{\text{IAA}}, -\frac{(\rho_{\text{PIN}_0} + \rho_{\text{PIN}}a^*)\kappa_{\text{PIN}}}{(1 + \kappa_{\text{PIN}}a^*)^2} - \mu_{\text{PIN}} \right\}$$

Since the parameters are assumed to be positive with the exception of ρ_{PIN_0} which is nonnegative (see also Table 5.1) we do not have a zero eigenvalue.

The inverse of $\boldsymbol{\pi}'(\mathbf{y}^*) - \boldsymbol{\delta}'(\mathbf{y}^*)$ can be computed explicitly and for $T \ll 1 \mu\text{m}^3/\text{h}$ we obtain to leading order

$$a_i = \begin{cases} a^* & \text{for } i = 1 \dots n-2, \\ a^* + \frac{pT}{2V} \left[\frac{\rho_{\text{IAA}}\kappa_{\text{IAA}}}{1 + \kappa_{\text{IAA}}(a^*)^2} + \mu_{\text{IAA}} \right]^{-1} \frac{(a^*)^2}{1 + \kappa_T(a^*)^2} & \text{for } i = n-1, \\ a^* - \frac{pT}{2V} \left[\frac{\rho_{\text{IAA}}\kappa_{\text{IAA}}}{1 + \kappa_{\text{IAA}}(a^*)^2} + \mu_{\text{IAA}} \right]^{-1} \frac{(a^*)^2}{1 + \kappa_T(a^*)^2} & \text{for } i = n, \end{cases}$$

$$p_i = \begin{cases} p^* & \text{for } i = 1 \dots n-2, \\ p^* + \frac{pT}{2V} \frac{\left[\frac{\rho_{\text{PIN}}}{1 + \kappa_{\text{PIN}}p^*} \right] \left[\frac{(a^*)^2}{1 + \kappa_T(a^*)^2} \right]}{\left[\frac{\rho_{\text{IAA}}\kappa_{\text{IAA}}}{(1 + \kappa_{\text{IAA}}a^*)^2} + \mu_{\text{IAA}} \right] \left[\frac{(\rho_{\text{PIN}_0} + \rho_{\text{PIN}}a^*)\kappa_{\text{PIN}}}{(1 + \kappa_{\text{PIN}}p^*)^2} + \mu_{\text{PIN}} \right]} & \text{for } i = n-1, \\ p^* - \frac{pT}{2V} \frac{\left[\frac{\rho_{\text{PIN}}}{1 + \kappa_{\text{PIN}}p^*} \right] \left[\frac{(a^*)^2}{1 + \kappa_T(a^*)^2} \right]}{\left[\frac{\rho_{\text{IAA}}\kappa_{\text{IAA}}}{(1 + \kappa_{\text{IAA}}a^*)^2} + \mu_{\text{IAA}} \right] \left[\frac{(\rho_{\text{PIN}_0} + \rho_{\text{PIN}}a^*)\kappa_{\text{PIN}}}{(1 + \kappa_{\text{PIN}}p^*)^2} + \mu_{\text{PIN}} \right]} & \text{for } i = n. \end{cases}$$

6.0.3. Two-dimensional domain of identical hexagonal cells. Lemma 6.1 applies when the Smith et al. model is posed on a two-dimensional array of identical hexagonal cells. In this case, the computations for \mathbf{y}^* are identical to the previous example and the asymptotic derivation is also straightforward: in the one dimensional case with Neumann boundary conditions at $i = 1$ and free boundary conditions at $i = n$ we have $\xi_i = 0$ for $i = 1, \dots, n-2$ and $\xi_{n-1,n} = \mp 1/2$, which leads to the pre-factors $\pm 1/2$ in the final expressions for a_i and p_i . For hexagonal cells, these pre-factors have to be re-calculated. Instead of writing the full expressions for \mathcal{B} , \mathcal{I} and $\boldsymbol{\xi}$, we refer the reader to Figure 6.1, where the values of $\boldsymbol{\xi}$ are shown for two corners of the domain. As claimed in the main text, the highest peaks occur at the top-left and right-bottom corners.

7. Models with diffusion. DEFINITION 7.1 (Concentration-based model with diffusion). *A concentration-based model with diffusion is a set of mn ODEs of the form*

$$\dot{\mathbf{y}}_i = \boldsymbol{\pi}(\mathbf{y}_i) - \boldsymbol{\delta}(\mathbf{y}_i) + \mathbf{D} \sum_{j \in \mathcal{N}_i} (\mathbf{y}_j - \mathbf{y}_i) + T \sum_{j \in \mathcal{N}_i} \boldsymbol{\nu}_{ji}(\mathbf{y}_1, \dots, \mathbf{y}_n) - \boldsymbol{\nu}_{ij}(\mathbf{y}_1, \dots, \mathbf{y}_n), \quad (7.1)$$

for $i = 1, \dots, n$, where $\mathbf{D} \in \mathbb{R}^{m \times m}$ is a diagonal diffusion matrix and all other quantities are as in Definition 6.1

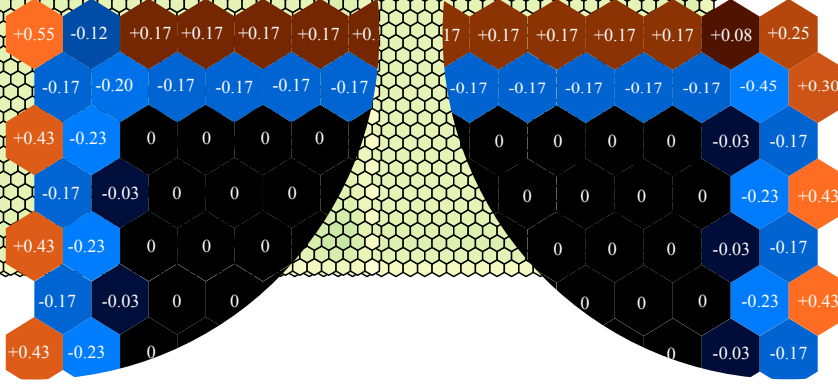


FIG. 6.1. Geometric pre-factors ξ_i at the top-left and top-right corners of a 50 by 50 array of identical hexagonal cells with 4 neighbours at the left and right edges and 3 neighbours at the top and right edges (see main text for further details). The interior set \mathcal{I} is now clearly visible. Peaks and dips are proportional, for small T and $D = 0$, to the values of ξ_i . When $D \neq 0$ the largest peak is formed in the interior, close to the top/left corner and a smaller one is formed in the interior, towards the top/right corner (see main text).

REMARK 7.1. Reasoning like in Lemma 6.1, we pose $\mathbf{D} = T\tilde{\mathbf{D}}$ and obtain $\mathbf{y}_i = \mathbf{y}^* + \boldsymbol{\eta}_i$ where $\boldsymbol{\eta}_i$ satisfy

$$\left(\mathbf{J}(\mathbf{y}^*) + \mathbf{L} \otimes \tilde{\mathbf{D}}\right) \begin{bmatrix} \boldsymbol{\eta}_1 \\ \vdots \\ \boldsymbol{\eta}_n \end{bmatrix} = \begin{bmatrix} \xi_1 \psi(\mathbf{y}^*, \mathbf{y}^*) \\ \vdots \\ \xi_n \psi(\mathbf{y}^*, \mathbf{y}^*) \end{bmatrix},$$

$\mathbf{J}(\mathbf{y}) \in \mathbb{R}^{mn \times mn}$ is block-diagonal with blocks $\boldsymbol{\pi}'(\mathbf{y}^*) - \boldsymbol{\delta}'(\mathbf{y}^*)$, $\mathbf{L} \in \mathbb{R}^{n \times n}$ is the Laplacian matrix associated to the graph G with Neumann boundary conditions and \otimes denotes the Kronecker product between matrices. The operator $\mathbf{L} \otimes \tilde{\mathbf{D}}$ is negative semi-definite and it has a zero eigenvalue, corresponding to a constant eigenvector. However, summing this matrix to $\mathbf{J}(\mathbf{y}) = \boldsymbol{\pi}'(\mathbf{y}^*) - \boldsymbol{\delta}'(\mathbf{y}^*)$, makes the resulting linear operator non-singular.

In the presence of diffusion we can not directly apply the formula (6.4), even for regular cellular arrays: owing to diffusion, cells in \mathcal{I} will also deviate from the homogeneous state, hence peaks and dips are not necessarily formed within \mathcal{B} , but may occur in interior cells that are close to the boundary. First-order corrections for these cases should be computed with linear algebra routines solving a simple linear problems. Even though we report below an example of this calculation, we point out that in practice this is not necessary, since the numerical bifurcation software gives access to the full nonlinear solution and to its linear stability.

7.0.4. One-dimensional domain with diffusion and two components per cell. We return to the Smith et al. model with $m = 2$, posed on a row of identical cells, and we now add diffusion only in the auxin component.

The expressions for a^* and p^* are unchanged from Section 6.0.2, as is the first order approximation of p_i (since there is no diffusion for p). Expressions for the first-order approximations in a_i are more involved: proceeding as explained above for

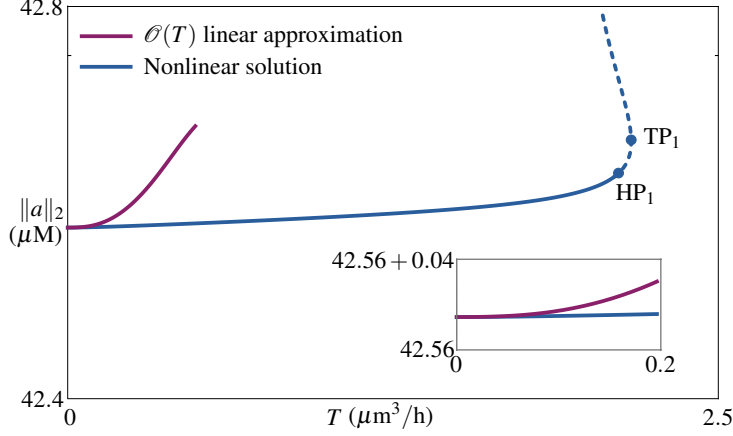


FIG. 7.1. Comparison between a branch of approximate linear $\mathcal{O}(T)$ solutions (magenta) and the corresponding branch of solutions to the full 2-component nonlinear system by Smith et al. (blue) for a row of 150 identical cells with homogeneous Neumann boundary conditions at $i = 0$ and free boundary conditions at $i = n$. The plot shows the 2-norm of the IAA concentration vector versus the continuation parameter T . All other parameters are as in Table 5.1.

generic models with diffusion, we obtain, to leading order

$$\left[\begin{array}{c} \left(\frac{\rho_{\text{IAA}} \kappa_{\text{IAA}}}{(1 + \kappa_{\text{IAA}} a^*)^2} + \mu_{\text{IAA}} \right) \begin{pmatrix} 1 & 0 & \dots & \dots & 0 \\ 0 & 1 & 0 & \dots & 0 \\ & & \ddots & & \\ & & & \ddots & \\ 0 & \dots & \dots & 0 & 1 \end{pmatrix} + \frac{TD}{V} \begin{pmatrix} -1 & 1 & & & \\ 1 & -2 & 1 & & \\ & \ddots & \ddots & \ddots & \\ & & 1 & -2 & 1 \\ & & & 1 & -1 \end{pmatrix} \\ \begin{pmatrix} \eta_1 \\ \eta_2 \\ \vdots \\ \vdots \\ \eta_n \end{pmatrix} = \begin{pmatrix} \xi_1 \psi(\mathbf{a}^*, \mathbf{p}^*) \\ \xi_2 \psi_2(\mathbf{a}^*, \mathbf{p}^*) \\ \vdots \\ \vdots \\ \xi_n \psi_n(\mathbf{a}^*, \mathbf{p}^*) \end{pmatrix} = \begin{pmatrix} 0 \\ \vdots \\ 0 \\ \frac{1}{2} \psi_{n-1}(\mathbf{a}^*, \mathbf{p}^*) \\ -\frac{1}{2} \psi_n(\mathbf{a}^*, \mathbf{p}^*) \end{pmatrix} \end{array} \right].$$

In Figure 1 of the main text we plot approximate solution profiles \mathbf{a} obtained solving the linear equation above for a row of 150 identical cells, $T = 3 \cdot 10^{-5} \mu\text{m}^3/\text{h}$ and various values of D .

We remark that this solution is only an approximation valid for $T \ll 1 \mu\text{m}^3/\text{h}$. In Figure 7.1 we compare a branch of approximate solutions (magenta) to a branch of solutions to the full nonlinear problem (blue) for $D = 1 \mu\text{m}^2/\text{h}$ and small values of T . We have an excellent agreement for $T \leq 0.2 \mu\text{m}^3/\text{h}$ (see inset), after which the two branches depart from each other as expected. In Figure 7.2 we show spectra of solutions around selected bifurcation points on the fully nonlinear solution branch, corresponding to Figures 2 and 3 in the main text.

8. Periodic solution close to HP1. As we have seen in the main text, the Smith et al. model posed on a row of cells admits steady states with one or more peaks at the boundary. Such states undergo a sequence of oscillatory instabilities along the snaking bifurcation diagram. We expect branches of periodic solutions to

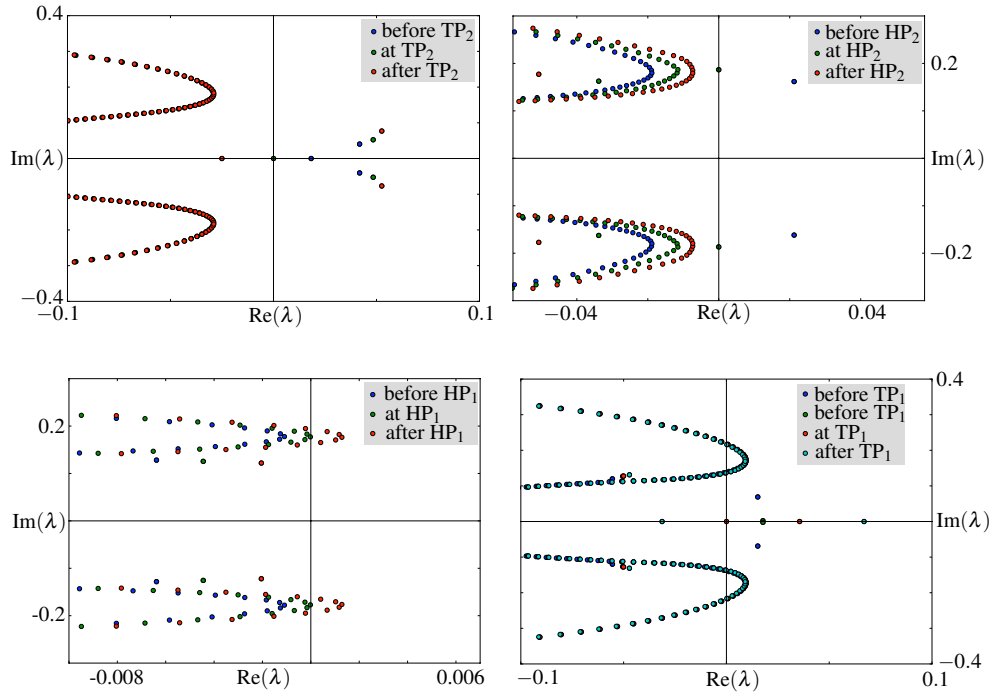


FIG. 7.2. Spectra of solutions around selected bifurcation points found as the snaking bifurcation branch is ascended (see Figure 2 in the main text). Parameters as in Table 5.1.

exist close to Hopf bifurcations in the snaking bifurcation curve. In Fig. 8.1 we show a periodic solution obtained via time simulation in the neighbourhood of HP_1 (which is also visible in Figure 7.1 of the supplementary material). We set $T \gtrsim T_{HP_1}$ and use as initial condition a steady state (with one peak at the boundary), obtained for $T \lesssim T_{HP_1}$. In the resulting periodic state, auxin peaks are dynamically formed from the tip towards the interior of the domain: we point out that the period of oscillations (about 377 hours) is much greater than the period associated to the unstable Hopf eigenvalues. In addition, on such long time scales it is reasonable to assume that new cells are formed, so the geometry of the problem should change as well.

References.

- [1] Scarpella E, Marcos D, Friml J, Berleth T. 2006. Control of leaf vascular patterning by polar auxin transport. *Genes & Development* **20**:1015-1027.
- [2] L. R. Band, D. M. Wells, A. Larrieu, J. Sun, A. M. Middleton, A. P. French, G. Brunoud, E. Mendocilla Sato, M. H. Wilson, B. Pret, et al. Root gravitropism is regulated by a transient lateral auxin gradient controlled by a tipping-point mechanism, *PNAS*, **09 (12)**: 4668-4673, 2012.
- [3] Lavenus J, Goh T, Roberts I, Guyomarc'h S, Lucas M, De Smet I, Fukaki H, Beeckman T, Bennett M, Laplaze L. 2013. Lateral root development in Arabidopsis: fifty shades of auxin. *Trends in Plant Science* **18**:450-458
- [4] de Wit M, Lorrain S, Fankhauser C. 2013. Auxin-mediated plant architectural changes in response to shade and high temperature. *Physiol Plant*
- [5] Smith RS, Guyomarc'h S, Mandel T, Reinhardt D, Kuhlemeier C, Prusinkiewicz P. 2006. A plausible model of phyllotaxis. *PNAS* **103(5)**:1301-1306.

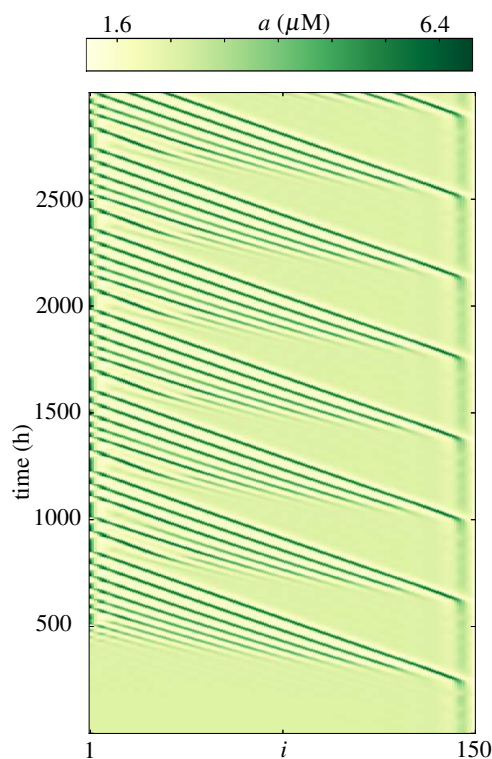


FIG. 8.1. Spatio-temporal state obtained via time simulation of the Smith *et al.* model posed on a one-dimensional domain, close to the Hopf bifurcation HP_1 (see main text). We set $T \gtrsim T_{HP_1}$ (and other parameters as in Table 5.1) and use as initial condition a steady state with one peak at the boundary, obtained for $T \lesssim T_{HP_1}$. A long-time periodic auxin wave travels (and new auxin peaks are recruited) from the tip towards the proximal part of the domain.

- [6] de Reuille PB, Bohn-Courseau I, Ljung K, Morin H, Carraro N, Godin C, Traas J. 2006. Computer simulations reveal properties of the cellcell signaling network at the shoot apex in Arabidopsis. *PNAS* **103(5):1627-1632**.
- [7] Jönsson H, Heisler MG, Shapiro BE, Meyerowitz EM, Mjolsness E. 2006. An auxin-driven polarized transport model for phyllotaxis. *PNAS* **103(5):1633-1638**.
- [8] Grieneisen VA, Xu J, Maree AF, Hogeweg P, Scheres B. 2007. Auxin transport is sufficient to generate a maximum and gradient guiding root growth. *Nature* **449:1008-1013**
- [9] Jones A.R., Kramer E., Knox K., Swarup R., Bennett M.J., Lazarus C.M, Ottoline Leyser, H. M., Grierson, C.S. 2008. Auxin transport through non-hair cells sustains root-hair development. *Nature Cell Biology* **11:78-84**.
- [10] Brena-Medina, V., Champneys, A. R., Grierson, C. and Ward, M.J. 2013. Mathematical Modelling of Plant Root Hair Initiation: Dynamics of Localized Patches. *SIAM J. Appl. Dyn. Syst.* **13(1), 210–248**.
- [11] Berleth T, Scarpella E, Prusinkiewicz P. 2007. Towards the systems biology of auxin transport-mediated patterning. *Trends in Plant Science* **12:151-159**
- [12] Stoma S, Lucas M, Chopard J, Schaedel M, Traas J, Godin C. 2008. Flux-Based Transport Enhancement as a Plausible Unifying Mechanism for Auxin Transport in Meristem Development. *PLoS Computational Biololgy* **4:e1000207**

- [13] Kramer EM, Bennett MJ. 2006. Auxin transport: a field in flux. *Trends in Plant Science* **11:382-386**
- [14] Wabnik K, Govaerts W, Friml J, Kleine-Vehn J. 2011. Feedback models for polarized auxin transport: an emerging trend. *Molecular bioSystems* **7:2352-2359**
- [15] Swarup R, Kramer EM, Perry P, Knox K, Leyser HM, Haseloff J, Beemster GTS, Bhalerao R, Bennett MJ. 2005. Root gravitropism requires lateral root cap and epidermal cells for transport and response to a mobile auxin signal. *Nature Cell Biology* **7:1057-1065**
- [16] Wabnik K, Kleine-Vehn J, Balla J, Sauer M, Naramoto S, Reinohl V, Merks RMH, Govaerts W, Friml J. 2010. Emergence of tissue polarization from synergy of intracellular and extracellular auxin signalling. *Molecular System Biology* **6**
- [17] Merks RM, Van de Peer Y, Inz D, Beemster GTS. 2007. Canalization without flux sensors: a traveling-wave hypothesis. *Trends Plant Sci.* **12: 384390**.
- [18] Mitchison GJ. 1981. The polar transport of auxin and vein patterns in plants. *Phil Trans R Soc Lond B* **295:461-471**.
- [19] Krupinski P, Jönsson H. 2010. Modeling auxin-regulated development. *Cold Spring Harb. Perspect. Biol.* **2:a001560**
- [20] Kramer EM. 2008. Computer models of auxin transport: a review and commentary. *Journal of Experimental Botany* **59(1):45-53**
- [21] Rolland-Lagan AG, Prusinkiewicz P. 2005. Reviewing models of auxin canalization in the context of leaf vein pattern formation in arabidopsis. *The Plant Journal* **44:854-865**.
- [22] L. R. Band, J. A. Fozard, C. Godin, O. Jensen, T. Pridmore, M. J. Bennett and J. R. King, Multiscale Systems Analysis of Root Growth and Development: Modeling Beyond the Network and Cellular Scales, *The Plant Cell Online*, **24(10): 3892–3906**, 2012.
- [23] Feugier FG, Mochizuki A, Iwasa Y. 2005. Self-organization of the vascular system in plant leaves: inter-dependent dynamics of auxin flux and carrier proteins. *Journal of Theoretical Biology* **236:366-375**.
- [24] Kramer EM, Rutshow HL, Mabie SS. 2011. AuxV: a database of auxin transport velocities. *Trends in Plant Science* **16:461-463**
- [25] Steinacher A, Leyser O, Clayton RH. 2012. A computational model of auxin and pH dynamics in a single plant cell. *Journal of Theoretical Biology* **296:84-94**.
- [26] Heisler MG, Jönsson H. 2006. Modeling auxin transport and plant development. *Journal of Plant Growth Regulation* **25:302-312**.
- [27] Benková E, Michniewicz M, Sauer M, Teichmann T, Seifertová D, Jürgens G, Friml J. 2003. Local, efflux-dependent auxin gradients as a common module for plant organ formation. *Cell* **115:591-602**.
- [28] Bilsborough G, Runions A, Markoulas M, Jenkins H, Hasson A, Galinha C, Laufs P, Hay A, Prusinkiewicz P, Tsiantis M. 2011. Model for the regulation of arabidopsis thaliana leaf margin development. *Proceedings of the National Academy of Sciences* **108:3424-3429**.
- [29] Krauskopf B, Osinga HM and Galán-Vioque, J., Numerical Continuation methods for Dynamical Systems, Springer, 2007.
- [30] E. Knobloch. Spatially localized structures in dissipative systems: open problems. *Nonlinearity*, 21(4):T45–T60, 2008.
- [31] P. Woods and A. Champneys. Heteroclinic tangles and homoclinic snaking in the unfolding of a degenerate reversible hamiltonian-hopf bifurcation. *Physica D: Nonlinear Phenomena*, 129(3-4):147–170, 1999.

- [32] J. Burke and E. Knobloch. Homoclinic snaking: structure and stability. *Chaos*, 17(3):7102, 2007.
- [33] J. Burke and E. Knobloch. Snakes and ladders: localized states in the swift-hohenberg equation. *Physics Letters A*, 360(6):681–688, 2007.
- [34] M. Beck, J. Knobloch, D. Lloyd, B. Sandstede, and T. Wagenknecht. Snakes, ladders, and isolas of localised patterns. *SIAM J. Math. Anal.*, 41(3):936–972, 2009.
- [35] S. Chapman and G. Kozyreff. Exponential asymptotics of localized patterns and snaking bifurcation diagrams. *Physica D*, 238:319–354, 2009.
- [36] D. Lloyd, B. Sandstede, D. Avitabile, and A. Champneys. Localized hexagon patterns of the planar Swift–Hohenberg equation. *SIAM J. Appl. Dynam. Syst.*, 7:1049–1100, 2008.
- [37] D. Avitabile, D. Lloyd, J. Burke, E. Knobloch, and B. Sandstede. To snake or not to snake in the planar swift-hohenberg equation. *SIAM J. Appl. Dyn. Syst.*, 9:704–733, 2010.
- [38] C. Beaume, A. Bergeon, E. Knobloch. Convectons and secondary snaking in three-dimensional natural doubly diffusive convection. *Physics of fluids*, 25(024105), 2013.
- [39] D. L. Jacono, A. Bergeon, E. Knobloch, et al. Three-dimensional spatially localized binary-fluid convection in a porous medium. *Journal of Fluid Mechanics*, 730, 2013.
- [40] C. Taylor and J. H. Dawes. Snaking and isolas of localised states in bistable discrete lattices. *Physics Letters A*, 375(1):14–22, 2010.
- [41] S. Coombes, G. Lord, and M. Owen. Waves and bumps in neuronal networks with axo-dendritic synaptic interactions. *Physica D: Nonlinear Phenomena*, 178(3-4):219–241, 2003.
- [42] C. Laing and W. Troy. PDE methods for nonlocal models. *SIAM Journal on Applied Dynamical Systems*, 2(3):487–516, 2003.
- [43] J. Rankin, D. Avitabile, J. Baladron, G. Faye, and D. J. Lloyd. Continuation of localised coherent structures in nonlocal neural field equations. *SIAM Journal of Scientific Computing*, 2013, in press.
- [44] D. Avitabile, H. Schmidt. Snakes and ladders in an Inhomogeneous neural field model, 2014 *arXiv:1403.1037*
- [45] Brunoud G, Wells DM, Oliva M, Larrieu A, Mirabet V, Burrow AH, Beeckman T, Kepinski S, Traas J, Bennett MJ, et al.. 2012. A novel sensor to map auxin response and distribution at high spatio-temporal resolution. *Nature* **482**: 103-106.
- [46] Beemster GTS, Baskin TI. 1998. Analysis of cell division and elongation underlying the developmental acceleration of root growth in *Arabidopsis thaliana*. *Plant Physiology* **116**: 515-526.
- [47] Palme K, Gälweiler L. 1999. Pin-pointing the molecular basis of auxin transport. *Current Opinion in Plant Biology* **2(5)**:375-381.
- [48] Arfken G, Brown G, Weber H-J, Ruby, L. 1985, *Mathematical methods for physicists*, Academic Press, New York.
- [49] Draelants D, Broeckhove J, Beemster TSG, Vanroose W. 2012. Numerical bifurcation analysis of the pattern formation in a cell based auxin transport model. *Journal of Mathematical Biology* DOI 10.1007/S00285-012-0588-8
- [50] J. Burke and J. H. Dawes. Localized states in an extended swift-Hohenberg equation. *SIAM Journal on Applied Dynamical Systems*, 11(1):261–284, 2012.

- [51] E. Farcot, Y. Yuan Homogeneous Auxin Steady States and Spontaneous Oscillations in Flux-Based Auxin Transport Models, *SIAM Journal of Applied Dynamical Systems* **12(3):1330-1353**, 2013.
- [52] Merks RMH, Guravage M, Inzé D, Beemster GTS. 2011. VirtualLeaf: An Open-Source Framework for Cell-Based Modeling of Plant Tissue Growth and Development. *Plant Physiology* **155(2):656-666**.
- [53] Heisler MG, Ohno C, Das P, Sieber P, Reddy G, Long JA, Meyerowitz EM. 2005. Patterns of Auxin Transport and Gene Expression during Primordium Development Revealed by Live Imaging of the Arabidopsis Inflorescence Meristem. *Current Biology* **15:1899-1911**. (<http://www.sciencedirect.com/science/article/pii/S0960982205012133>)